Materials Advances

ROYAL SOCIETY OF CHEMISTRY

PAPER

Check for updates

Eradication of planktonic bacteria by shape-tailored gold nanoparticle photothermia†

Zhendong Peng, [a] Laurent Royon,[b] Yun Luo,[c] Philippe Decorse,[a]
Sarra Gam Derouich,[a] Michaël Bosco,[c] Christine Gravier-Pelletier,[c]
Romain Briandet,[d] John S. Lomas,[a] Claire Mangeney[c] and
Miryana Hémadi *[a]

Bacterial antimicrobial resistance (AMR) has emerged as a global challenge, exacerbated by the formation of biofilms. To address this issue, the bactericidal effect of gold nanoparticle photothermia has been explored. Gold nanoparticles with different morphologies: spherical (AuNSP), rods (AuNRO), stars (AuNST), and flower-shaped (AuNFL) were synthesised and characterised. Scanning and transmission electron microscopy images confirm the morphologies and give dimensions for the different types of nanoparticles in good agreement with those from dynamic light scattering measurements. Their photothermal capacities under irradiation at 808 and 1064 nm were assessed. The specific absorption rates were determined, and light-to-heat conversion efficiencies evaluated in the heating and cooling phases. Phothermally induced localized hyperthermia significantly increased the mortality rate of planktonic *Escherichia coli* in the stationary phase, approaching 100% for AuNRO, AuNST, and AuNFL, while AuNSP was ineffective. This demonstrates that bactericidal efficacy is highly dependent on nanoparticle morphology. These findings highlight the potential of shape-tailored gold nanoparticles for developing effective antibacterial treatments.

1. Introduction

The medicinal applications of gold, in metallic form, as colloids or as salts, known collectively as "Gold Therapy", go back several millennia. Early preparations would have been, at the best, placebos and at the worst, highly toxic.[1] In the 20th century gold compounds were proposed for the treatment of syphilis, tuberculosis, rheumatic diseases and inflammatory skin disorders but, because they were either ineffective or associated with severe side-effects, such therapies have been largely abandoned.[2] Current medical applications of colloidal gold concern primarily imaging and detection, notably of malaria, based on the ability of nanoparticles to adsorb proteins and DNA.[3,4] The escalating global challenge of bacterial resistance, fueled by antibiotic overuse and the rise of drug-resistant strains, presents a pressing concern. Projections suggest that drug-resistant microbes could lead to 10

million deaths annually by 2050.[5] Bacterial biofilm formation is critical to the development and propagation of bacterial resistance. Biofilms, intricate spatially-organized bacterial communities encapsulated in extracellular polymeric substances (EPS), diverge from their planktonic counterparts by adhering to surfaces, creating three-dimensional structures that enhance stability, and shield against antimicrobial actions, resulting in drug tolerance and localized chronic infections.[6]

Gold nanoparticles (AuNPs) are biocompatible, have large specific surface areas, easy-to-groom surfaces, high stability, excellent electrochemical properties, the ability to penetrate biofilms and interesting optical properties, notably in surface-enhanced Raman scattering (SERS).[7] The free electrons on the surface of gold resonate with laser irradiation of the appropriate wavelength, a phenomenon known as localized surface plasmon resonance (SPR). In the therpeutic medicinal applications of gold nanoparticles, *i.e.* applications other than detection and imaging, there are basically two approaches and two fields of concern. The approaches are photodynamic therapy (PDT) and photothermal therapy (PTT), and the fields are cancer and bacterial infections.[8,9] Without going into details of these therapies, which have been largely reviewed elsewhere,[10] it is enough to say that PDT involves the release of reactive oxygen species (ROS) while PTT produces localized heating, both by light irradiation. In either case, the nanoparticles used

[a] *Université Paris Cité, CNRS-UMR 7086, Interfaces, Traitements, Organisation et DYnamique des Systèmes (ITODYS), Paris, France. E-mail: hemadi@u-paris.fr; Tel: +33-1-55278839*

[b] *Université Paris Cité, CNRS-UMR 8236, LIED, F-75013 Paris, France*

[c] *Université Paris Cité, CNRS-UMR 8601, LCBPT, F-75006 Paris, France*

[d] *Université Paris Saclay, INRAE, AgroParisTech, Micalis Institute, F-78350 Jouy-en-Josas, France*

can be functionzalised with molecules that have their own therapeutic activity and are released into the target cells, leading thereby to synergistic effects.[11,12] Despite a great deal of work on the reduction of tumors by PTT this technique has not reached the status of a regular procedure in cancer therapy, whereas PDT is routinely used on cancers not only of the skin but also of other less accessible sites.[13,14] AuNP-mediated PDT and PTT have bactericidal effects *in vitro* and *in vivo* but there have been few systematic studies on the efficacity of different types and sizes of AuNPs.[15] For PTT the critical factor is the photothermal efficiency, *i.e.* the extent to which light energy is transformed into heat, and most current knowledge in this field is derived from cancer-related studies. The surface chemistry, size and shape of AuNPs modulate the optical and electronic characteristics.[16,17] For example, the anticancer properties of anisotropic gold nanoparticles synthesized *via* silk fibroin were better than those of spherical nanoparticles.[18]

In this work, we focus on AuNPs of different morphologies: spherical, rod-shaped, star-shaped, and flower-like, designated as AuNSP, AuNRO, AuNST, and AuNFL, respectively (Table 1). Gold nanospheres (AuNSPs) are uniform spherical particles that appear burgundy-red when suspended in water. They were among the first gold nanoparticles used widely, due to their unique optical properties, making them valuable in disease detection, rapid antigen tests, and treatments.[19] In contrast, gold nanorods (AuNROs) are anisotropic and have tunable surface plasmon resonance, offering variable efficiency in converting light to heat.[20] Techniques such as seed growth allow precise control over their shape and surface chemistry, crucial for biomedical applications. Initially stabilized by CTAB, which is toxic, they are now stabilized by citrate.[21,22] Gold nanoflowers (AuNFLs) feature a porous, flower-like structure capable of absorbing light across a broad spectrum, including near-infrared (NIR) wavelengths. They find applications in SERS detection, imaging, photothermal therapy, and catalysis.[23] Lastly, gold nanostars (AuNSTs) have a spherical core with multi-crystalline tips, enhancing their ability to capture and

utilize light, particularly in the NIR range, making them effective as light antennas and for boosting electromagnetic fields at their tips.[24]

These AuNPs are synthesised and elaborated by well established procedures. Several characterisation techniques are used: scanning and transmission electron microscopy (SEM and TEM), Fourier-transform infrared spectroscopy (FTIR), X-ray photoelectron spectroscopy (XPS), dynamic light scattering (DLS), and visible-NIR spectroscopy. Photothermal capacities are expressed in terms of the specific absorption rate (SAR) and the light-to-heat conversion efficiency (η), and bactericidal activities are evaluated on planktonic bacteria (*Escherichia coli*) in the stationary phase.
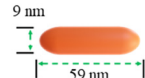
2. Materials and methods

2.1 Materials
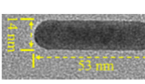
Chloroauric acid trihydrate (HAuCl$_4$·3H$_2$O, 99%), sodium citrate (Na$_3$C$_6$H$_5$O$_7$, 99%), cetyltrimethylammonium bromide (CTAB, 99%), sodium borohydride (NaBH$_4$, 98%), silver nitrate (AgNO$_3$, 99%), L-ascorbic acid (C$_6$H$_8$O$_6$, 99%), trisaminomethane–HCl (Tris–HCl), NaOH, dopamine, polyvinyl–pyrrolidone (PVP, 40 kDa) and polystyrene sulfonate (PSS) were purchased from Sigma-Aldrich and used as received.

2.2 Synthesis

Standard procedures were used for the preparation of the different types of AuNPs. All solutions were prepared in ultrapure water (Millipore, 18.2 MΩ).[25]

2.2.1 Spherical gold nanoparticles (AuNSP): citrate-capped[26]. HAuCl$_4$ solution (100 mM, 0.5 mL) was added to 50 mL of water and heated to boiling with magnetic stirring. Sodium citrate solution (39 mM, 5 mL) was then added. The solution darkened and gradually turned red. After 30 minutes the mixture was cooled to room temperature and stored at 4 °C. Au^0 concentration is approximately 0.9 mM.

Table 1 Synthesis methods, hydrodynamic diameters by DLS, zeta potentials, and XPS results for AuNSP–citrate, AuNRO–CTAB, AuNFL–dopamine and AuNST–PVP

			NanoSPheres	NanoROds		NanoFLowers	NanoSTars
Synthesis method			Turkevich method	Seed growth method		Seed growth method	Silver-assisted method
Reducer			Sodium citrate	Ascorbic acid		Dopamine	Ascorbic acid
Capping agent			Citrate	CTAB	Citrate	Dopamine	PVP
Shape (hydrodynamic diameter, DLS)			(18 nm)	(9 nm / 59 nm)		(96 nm)	(106 nm)
Polydispersity			0.156	0.542		0.097	0.023
Shape (diameter, TEM)			(15 nm)	(51 nm)		(90 nm)	(98 nm)
Zeta potential (mV)			−40.2 ± 0.5	37.0 ± 0.6	−40.0 ± 4.1	−23.1 ± 0.5	−36.8 ± 0.8
XPS	O/C	Exp	0.9	0.04	0.25	0.18	0.51
		Theo	1.2	0	1.2	0.17	0.25
	N/C	Exp	0	0.05	0.12	0.18	0.19
		Theo	0	0.05	0	0.17	0.13

2.2.2 Gold nanorods (AuNRO): CTAB-capped[27]. CTAB solution (200 mM) was prepared by dissolving the appropriate amount of CTAB in water at 30 °C with gentle stirring to prevent foam formation. To prepare the seed solution, CTAB solution (5 mL) was diluted with water (4.75 mL) and $HAuCl_4$ solution (10 mM, 0.25 mL) added. Under vigorous stirring, pre-cooled $NaBH_4$ solution (10 mM, 0.3 mL) was added to the mixture. After 2 minutes, the solution was incubated for 2 hours at 30 °C.

Meanwhile, CTAB solution (200 mM, 50 mL) was mixed with water (49.5 mL) and $HAuCl_4$ solution (100 mM, 0.5 mL) added. The mixture was stirred until it turned yellow-brown. Then, $AgNO_3$ (10 mM, 1 mL) was added, followed by the rapid addition of ascorbic acid (100 mM, 0.55 mL). The growth solution immediately turned colourless. Freshly prepared seed solution (0.12 mL) was added to the mixture, which was well stirred, then allowed to stand overnight at 30 °C. The AuNRO suspension was centrifuged (14 000 rpm, 30 minutes), and the supernatant decanted, resuspended in water (10 mL), and stored at 30 °C. Au^0 and Ag^0 concentrations are approximately 0.49 mM and 0.1 mM, respectively.

2.2.3 Gold nanorods (AuNRO): citrate-capped[21]. A sample of the above-prepared AuNRO suspension (5 mL) was dispersed in a solution of PSS in water (0.15 wt%, 20 mL), mixed well, incubated for 1 hour, centrifuged and redispersed in PSS solution; the process was repeated 3 times. The PSS-capped AuNROs were dispersed in sodium citrate solution (5 mM, 20 mL), incubated for 12 hours, centrifuged and redispersed in sodium citrate; the process was repeated twice. The resulting citrate-capped AuNROs were resuspended in citrate solution (5 mM) at 4 °C for storage.

2.2.4 Gold nanoflowers (AuNFL): dopamine-capped[23]. Tris–HCl buffer was prepared by dissolving an appropriate amount of Tris–HCl in water and adjusting the pH to 8.5 with 1 N NaOH. Buffer (16 mL) was degassed with argon for 15 minutes and previously synthesised AuNSPs (0.1 mL) were added with magnetic stirring, followed by dopamine (4 mg mL^{-1}, 0.1 mL) and $HAuCl_4$ solution (10 mM, 0.5 mL). The colour changed immediately from light pink to orange-yellow and gradually to black. The reaction was allowed to proceed in a closed vessel for 6 hours and the suspension, approximately 0.3 mM in Au^0, was stored at 30 °C.

2.2.5 Gold nanostars (AuNST): PVP-capped. $HAuCl_4$ solution (10 mM, 0.4 mL) was diluted in water (20 mL). Simultaneously $AgNO_3$ (10 mM, 0.04 mL) and ascorbic acid (100 mM, 0.08 mL) were added. The solution was stirred for 30 seconds, then PVP_{40k} (1 wt%, 0.02 mL) was added and the solution stirred for a further 5 minutes, after which it was stored at 4 °C. Au^0 and Ag^0 concentrations are approximately 0.2 mM and 0.02 mM, respectively.

2.3 Characterisation techniques

The physical and optical properties of the AuNPs synthesised were characterised by electron microscopy and various spectroscopic techniques, and their photothermal properties were studied.

2.3.1 Visible-NIR absorption spectroscopy. The Vis-NIR absorption spectra of AuNP suspensions were recorded on an Agilent Cary 4000 and a PerkinElmer Lambda 1050 spectrophotometers. All measurements were performed using a 1 cm quartz cuvette.

2.3.2 ATR-FTIR spectroscopy. ATR-FTIR spectra (500–4000 cm^{-1}) were recorded on a Thermo Nicolet-iS50 spectrometer equipped with an attenuated total reflectance (ATR) accessory. A small amount of the concentrated sample suspension was placed on the ATR sample stage and dried in air. Background correction was performed using air signals before each test.

2.3.3 Dynamic light scattering (DLS). Suspensions of AuNPs were diluted several times and ultrasonicated for 1 minute to remove air bubbles. The hydrodynamic diameter distribution and the charge on the AuNPs were then immediately measured on a Malvern Nano ZS with ultrapure water as the background electrolyte. Size distribution was determined with a Mobius disposable cuvette. For zeta potentials, the diluted AuNP suspensions (AuNSP–citrate, AuNRO–CTAB, AuNRO–citrate, AuNFL–dopamine, and AuNST–PVP) were injected into a DTS 1070 cuvette and scanned 100 times; each sample was run 3 times.

2.3.4 X-ray photoelectron spectroscopy (XPS). The superficial elemental composition of the nanomaterials was analysed on a K-Alpha+ spectrometer (ThermoFisher Scientific) equipped with a micro-focused, monochromatic Al Kα X-ray source (1486.6 eV, spot size: 400 µm) and a flood gun (charge compensation module for insulating samples). The step size and pass energy were set to 1 eV/200 eV and 0.1 eV/40 eV for the survey and the high resolution regions, respectively. Data acquisition and processing were performed with Avantage software, version 5.9902. The surface chemical composition was determined by using the manufacturer sensitivity factors. Typical sample preparation involved concentrating 1 mL of the AuNP suspension by centrifugation, discarding the supernatant, and gently transferring moist pellet material onto an indium tin oxide-coated conductive glass slide and allowing it to dry at room temperature; the process was repeated several times to ensure sufficient thickness for testing.

2.3.5 Transmission electron microscopy (TEM). The morphology and nanostructure of the AuNPs were characterised by TEM by means of a JEOL 2100+ electron microscope equipped with a LaB6 electron gun and an ultrascanning 2 K × 2 K CCD camera for high-resolution imaging. For sample preparation, AuNP suspensions were dropped onto a 200 mesh copper grid and allowed to dry at room temperature overnight. The particle size was analysed by ImageJ software (version 1.50i), counting no fewer than 50 particles.

2.3.6 Scanning electron microscopy (SEM). The surface morphologies of AuNPs were characterised by means of a Zeiss Gemeni SEM 360 electron microscope. For sample preparation, AuNP suspensions were dropped onto a silicon wafer and dried overnight at room temperature. The silicon wafers were fixed onto the sample holder with conductive carbon adhesive and images were obtained at an accelerating voltage of 5 kV.

2.4 Photothermal properties and bacterial investigations

The photothermal capacities of the different AuNPs were determined at two NIR wavelengths (808 nm and 1064 nm).

The bactericidal effect of these nanomaterials on planktonic bacteria was then examined with and without laser irradiation.

2.4.1 Photothermal properties. AuNP suspensions (100 μL, 0.05 mM < [Au⁰] < 0.2 mM), previously stabilised at room temperature, were irradiated for 5 min. in 0.5 mL polypropylene Eppendorf tubes at 808 nm and 1064 nm (laser spot diameter 0.3 cm, sources from Laser Components S.A.S., France). The laser-sample distance was set at 10 cm. The illuminated surface of the Eppendorf was 1.1 cm², and the laser power (continuous pulse mode) was set at 0.3 W or 0.5 W, so the power densities were 0.273 and 0.455 W cm⁻². The temperature variation was monitored by a FLIR A615 IR thermal-imaging camera (accuracy ±2% with a reference, sensitivity: <0.05 °C at +30 °C) until it reached a plateau, whereupon the laser was turned off and cooling was monitored for a further 3 minutes.

2.4.2 Biological investigations. Planktonic bacteria were first cultured and subsequently used to evaluate the bactericidal effects of the nanomaterials.[28,29]

2.4.2.1 Storing and culturing E. coli from −80 °C. The bacterial strain used in this study was *Escherichia coli* SS2,[30] this strain was chosen specifically due to its well-documented ability to form biofilms on inert surfaces, making it a model pathogen for biofilm-related research. *E. coli* SS2 stored in a −80 °C freezer was sampled by an inoculating loop, mixed with sterilised Tryptic Soy Broth (TSB) medium and incubated at 37 °C overnight. The culture (0.2 mL) was mixed with fresh TSB (10 mL) and spread on Tryptic Soy Agar (TSA) solid medium plate using the streak-plate method. The plate was incubated overnight at 37 °C. Colony morphology was observed under a microscope, suitable colonies selected, diluted in TSB, and stored at 4 °C as stock suspension. This stock suspension was prepared immediately before use.

2.4.2.2 Plotting the growth curve of E. coli. *E. coli* stock suspension (0.2 mL) was diluted in TSB medium (20 mL), and the diluted culture was divided into 1 mL aliquots. The aliquots were incubated at 37 °C and one portion was taken out every 30 min to determine the absorbance at 600 nm using a glass cuvette; pure TSB medium was used as the reference. The exponential growth phase shows a steep upward curve, while the stationary phase appears as a plateau.

2.4.2.3 Bactericidal effect of AuNPs. The effect of photothermia by AuNPs of different morphologies on *E. coli in vitro* was investigated in the stationary phase. *E. coli* culture (0.2 mL) was diluted in TSB (20 mL) and incubated at 37 °C for 5 hours until it reached the stationary phase. It was then centrifuged at 5000 g for 10 minutes to collect the bacteria which were then redispersed in saline. AuNPs were centrifuged and resuspended in saline to obtain a 0.9 mM suspension of AuNSPs and 0.3 mM suspensions of AuNRO, AuNFL and AuNST. AuNPs suspensions (66.6 μL) were mixed with *E. coli* suspension (33.4 μL) to give final concentrations of 0.6 mM for AuNSP and 0.2 mM for the others, a higher concentration being used for AuNSP due to its lower photothermal capacity. The control group did not contain any AuNPs. The AuNP suspensions mixed with bacteria were incubated at 37 °C for 1 hour, allowed to cool to room temperature, then irradiated at 808 nm for 10 minutes at 0.5 W and cooled to 20 °C. Samples were immediately serially diluted 10-fold, and 4 sample spots (0.01 mL each) were dropped onto TSA plates and incubated at 37 °C for 24 hours. Sample spots of appropriate dilutions were selected to evaluate the bactericidal effect by counting the colony-forming units (CFU). The numbers of *E. coli* before and after treatment are expressed as $\log N$ (CFU mL⁻¹).

2.4.2.4 Bacterial mortality. The mortality is a direct measure of the efficacy of a treatment, representing the proportion of the initial population of bacteria that has been killed (eqn (1).

$$\% \text{ mortality} = \left(\frac{N_0 - N}{N_0}\right) \times 100 \tag{1}$$

where N_0 is the initial number of bacteria, *i.e.* the number of culturable bacteria before treatment and N the final number of bacteria, *i.e.* the number of culturable bacteria after treatment.

2.4.2.5 Statistics. The significance of the treatments was evaluated using *t*-tests for pairwise comparisons. To further validate these results, Tukey's multiple comparison test was applied using PRISM software (GraphPad, California, USA). The levels of significance are reported as follows: non-significant for $P > 0.05$, * for $P \le 0.05$ (significant), ** for $P \le 0.01$ (highly significant), *** for $P \le 0.001$ (very highly significant), and **** for $P \le 0.0001$ (extremely significant).

3. Results and discussion

3.1 Synthesis and characterisation

Gold nanoparticles with various morphologies, including gold nanospheres, nanorods, nanostars, and nanoflowers, were synthesised by established methods (Table 1).

SEM and TEM images of the different nanoparticles confirmed that they were of the correct morphologies (Fig. 1 and Fig. S1, ESI†). According to the TEM measurements, particle sizes were 15 nm for AuNSPs, 14 and 53 nm (transverse and longitudinal axes) for AuNROs, 90 nm for AuNFLs, and 98 nm for AuNSTs. Hydrodynamic diameters, determined by DLS measurements, were generally slightly higher. AuNSPs have an average diameter of 18 nm with a half-height width of about 20 nm. Values for AuNROs are 9 and 59 nm. Values for AuNFLs and AuNSTs reveal broad size distributions with average diameters of 96 nm and 106 nm, respectively. The polydispersities of the various morphologies, as determined by the DLS measurements, are generally low (0.02–0.16) except for the AuNROs (0.54) where the two size ranges cannot be separated (Table 1 and Fig. S2, ESI†).

Zeta potential measurements (Table 1) indicate a range of surface charges (−40 mV < ζ < +40 mV) depending on the capping agents. Citrate, PVP, and dopamine result in negative charges, while CTAB leads to positive charges. Despite these variations, all absolute values are sufficiently high to ensure suitable colloidal stability of the suspensions.
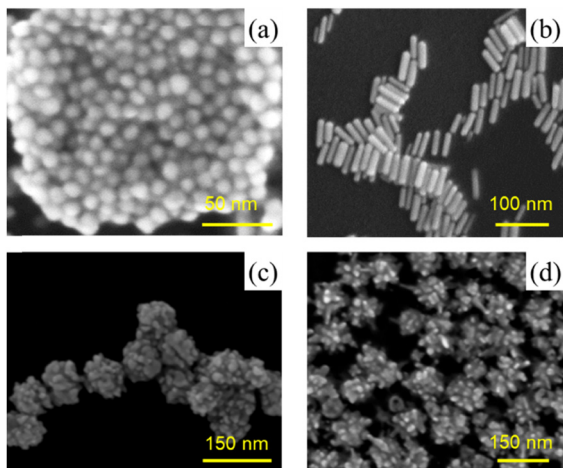
Fig. 1 SEM images of (a) AuNSP–citrate, (b) AuNRO–CTAB, (c) AuNFL–dopamine and (d) AuNST–PVP.

The surface chemical compositions of the AuNPs were investigated by XPS (Table 1 and Fig. S3, ESI†). The spectra reveal the presence of gold, along with varying amounts of carbon, oxygen and nitrogen, showing good agreement with previous work.[26,31–33] The theoretical N/C and O/C were compared with those determined experimentally. For AuNPS-citrate and, even better, AuNFL–dopamine there is good agreement between the values. For AuNST–PVP there is some disparity, with a notable lack of carbon, or an excess of nitrogen and oxygen, according to both ratios. The results for AuNRO–CTAB are adequate, despite the presence of a small amount of oxygen. The replacement of the CTAB by citrate to obtain AuNRO–citrate does not appear to have been complete: the O/C ratio is too low and the N/C ratio is too high. It is clear therefore that all the CTAB has not been replaced by citrate. A possible explanation is that residual CTAB near the core is being detected by the XPS analyses. However, the similarity of the zeta potentials for AuNSP–citrate and AuNRO–citrate suggests that citrate is the effective capping agent for the latter.

3.2 Optical properties of AuNPs of different morphologies

Fig. 2a shows the vis-NIR absorption spectrum of spherical gold nanoparticles (AuNSP) with a strong, sharp and symmetric SPR peak around 520 nm, reflecting their uniform spherical shape. Gold nanorods (AuNROs) show two distinct SPR absorption peaks: one at 520 nm, similar to that of AuNSPs but much weaker, due to the short axis and related to transverse SPR, and a stronger, broad band at 820 nm related to longitudinal SPR. The spectra of gold nanoflowers (AuNFLs) and gold nanostars (AuNSTs) are less well defined, featuring broad absorption bands over the entire range, due to their more complex structures.

The FTIR spectra of AuNPs (Fig. 2b) are primarily influenced by the surface chemistry and the morphology, which affect the adsorption of molecules and the enhancement of vibrational signals, as already well-established in the literature.[32–34] The FTIR spectra of the different morphologies show vibrational
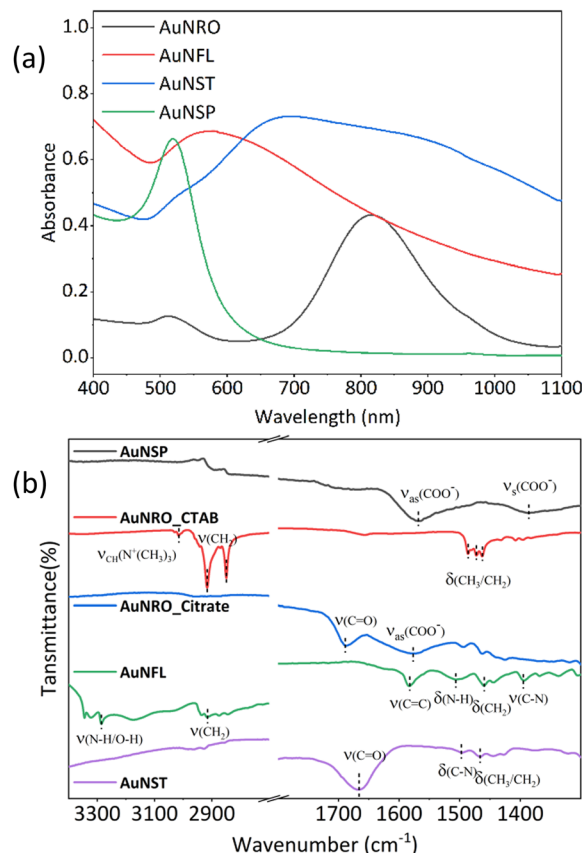
Fig. 2 (a) Vis-NIR absorption spectra (400–1100 nm) of AuNSP–citrate, AuNRO–CTAB, AuNFL–dopamine, and AuNST–PVP, $[Au^0]$ = 0.2 mM. (b) ATR-FTIR spectra of the same.

bands corresponding to the stabilising agents adsorbed on their surfaces: citrate (AuNSP, AuNRO), dopamine (AuNFL), PVP (AuNST) and CTAB (AuNRO).

3.3 Photothermal capacities of AuNP suspensions

Photothermal heating involves the use of specific materials, such as AuNPs, that can absorb light and convert it into heat. This technique is used to create localised high-temperature "hot spots" at the nanoscale level, in contrast to overall heating at the macroscopic level. This strategy could thus kill bacteria and destroy diseased cells without harming surrounding healthy tissue.[35,36]

The photothermal capacities of AuNPs are intrinsically related to their optical properties. Vis-NIR absorption spectra (Fig. S4, ESI†) of the different morphologies were recorded at three concentrations in order to evaluate their photothermal conversion efficiency. When the laser is switched on (808 nm or 1064 nm), the temperature of the AuNP suspension increases until a plateau is reached (Fig. S5, ESI†), whereupon the laser is turned off, and a cooling phase follows. The plateau at T_{max} corresponds to a state of equilibrium between the suspension with the surrounding environment (Fig. 3).

The AuNST, AuNRO, and AuNFL suspensions exhibit significant temperature increases, unlike that of AuNSPs. These increases

Fig. 3 Plateau temperatures reached after 5 min. of irradiation at 808 nm (a) or 1064 nm (b) of AuNP suspensions: AuNSP–citrate, AuNRO–citrate, AuNFL–dopamine, and AuNST–PVP, $[Au^0]$ = 0.2 mM.

Table 2 Comparative analysis of photothermal capacities of AuNRO–citrate, AuNFL–dopamine and AuNST–PVP with 0.3 W or 0.5 W irradiation at 808 nm

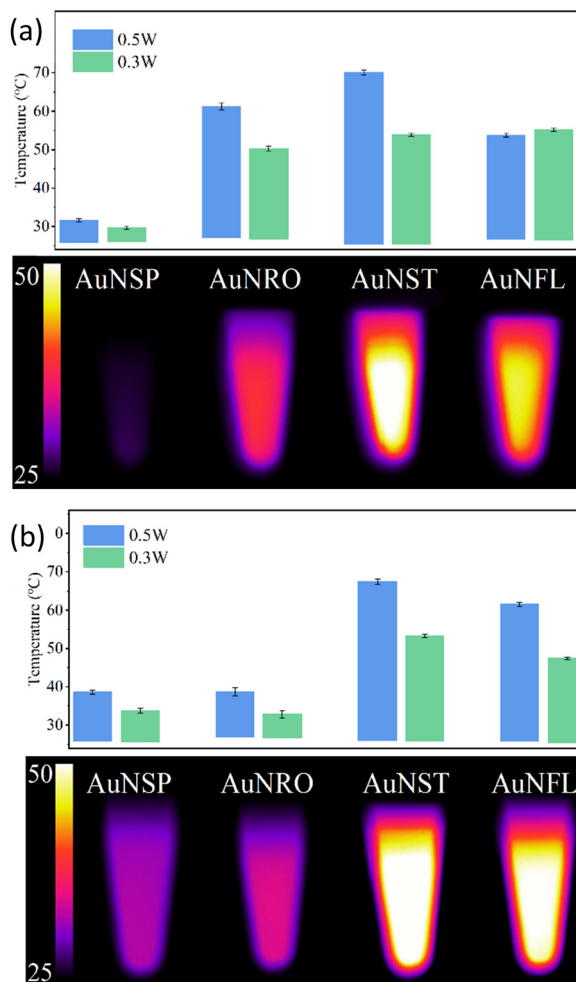| 808 nm	Power, W	$[Au^0]$, mM	ΔT, °C	SAR, W g^{-1}	τ_h, s	η_h, %	τ_c, s	η_c, %	η_{mean}, %
AuNRO	0.3	0.2	23.3	19 000	93	53	128	34	43
		0.1	13.9	20 300	94	48	135	29	38
		0.05	8.9	25 500	111	44	156	26	35
	0.5	0.2	34.0	28 700	88	48	119	31	40
		0.1	22.6	40 400	92	47	135	27	37
		0.05	12.3	40 800	98	39	137	23	32
AuNFL	0.3	0.2	26.9	27 100	98	57	139	40	49
		0.1	20.4	39 800	93	73	147	46	60
		0.05	17.0	80 700	113	82	133	69	75
	0.5	0.2	36.0	27 800	91	48	137	33	40
		0.1	31.1	44 600	92	66	143	43	55
		0.05	27.0	77 300	106	82	133	65	74
AuNST	0.3	0.2	31.3	20 600	101	60	131	46	53
		0.1	19.9	35 900	107	55	123	48	52
		0.05	11.7	33 100	127	45	135	42	44
	0.5	0.2	44.5	36 100	82	62	113	47	55
		0.1	30.2	53 100	94	56	123	44	50
		0.05	20.8	64 600	116	52.	143	48	50

where $\sum mC_p$ is the sum of the products of the mass and heat capacities of the sample components and $\left.\dfrac{dT}{dt}\right|_{t=0}$ represents the initial linear rate of temperature increase. Assuming that the mass of gold is negligible compared to that of water, we replace m by the mass of the sample (0.1 g) and C_p by $C_{p\text{-water}}$ (4.185 J g^{-1} K^{-1}). SAR corresponds to the heat power dissipated per unit mass (W g^{-1}) of nanoparticles (Table 2).

The photothermal capacity is better expressed by an analysis of the temperature profile during and after laser irradiation:[35,38,39]

Heating, laser on: $T_t = T_0 + \Delta T[1 - \exp(-t/\tau_h)]$, whence:

$$\mathrm{Ln}\frac{T_{max} - T_t}{T_{max} - T_0} = -\frac{t}{\tau_h} \qquad (3)$$

Cooling, laser off: $T_t = T_0 + \Delta T\exp(-t/\tau_c)$, whence:

$$\mathrm{Ln}\frac{T_t - T_0}{T_{max} - T_0} = -\frac{t}{\tau_c} \qquad (4)$$

where T_0 is the initial temperature, T_t is the temperature at time t, $\Delta T = T_{max} - T_0$, and τ_h and τ_c are the heating and cooling time coefficients, respectively.

At equilibrium, the thermal heat balance is given by eqn (5):

$$\sum mC_p\frac{dT}{dt} = Q_{in} - Q_{out} = Q_{NP} + Q_S - Q_{out} = 0 \qquad (5)$$

Q_S represents heating by the solvent. The entering heat flow (Q_{in}) is mainly given by nanoparticle heating:

$$Q_{NP} = I_0 - I_T = I_0(1-10^{-A_\lambda})\eta \qquad (6)$$

where I_0 and I_T are the incident and transmitted laser powers, respectively, A_λ represents the absorbance of the dispersion at the wavelength λ, and η is the light-to-heat conversion efficiency.

are consistent with the absorption spectra where, contrary to AuNSP, there are pronounced plasmonic effects in the AuNST, AuNRO, and AuNFL suspensions (Fig. 2a) at these wave-lengths (808 nm or 1064 nm). The weak photothermal effect in the AuNSP suspensions is consistent with their low absorbance in the NIR, and a similar behaviour is observed for the AuNRO suspensions at 1064 nm (Fig. 3). The AuNSP suspensions exhibit only minor heating (3–5 °C), mainly due to the warming of the water itself. Suspensions of all AuNPs were found to be photothermally stable over 3 cycles at both wavelengths, regardless of their capacities (Fig. S6, ESI†).

In this work, the photothermal capacities of AuNP suspensions are evaluated as reported elsewhere,[25,28,37] and are expressed by two parameters: the specific absorption rate (SAR, W g^{-1}) and the light-to-heat conversion efficiency (η).

The specific absorption rate is given by eqn (2):

$$\mathrm{SAR} = \frac{\sum mC_p}{m_{Au}}\left.\frac{dT}{dt}\right|_{t=0} \qquad (2)$$

The exiting heat flow (Q_{out}) is given by:

$$Q_{out} = hS(T_{max} - T_0) = \frac{\sum mC_p}{\tau}\Delta T \qquad (7)$$

where h is the heat transfer coefficient, S is the exchange surface and τ is the cooling or heating time coefficient.

The conversion efficiencies (η) are then calculated by eqn (8) for the cooling (τ_c) and heating (τ_h) processes (Table 2):

$$\eta = \frac{mC_p\Delta T - Q_s}{I_0(1 - 10^{-A_\lambda})\tau} \qquad (8)$$

where η expresses the ratio of the heat released by the nanoparticles to the energy absorbed.

In view of the previous results (absorption spectra and plateau temperature) with the AuNSP suspensions, their photothermal capacities at 808 nm and 1064 nm are very poor. Furthermore the absorption of AuNROs at 1064 nm is so low (Fig. 2a) that their photothermal capacity is of little interest. Therefore, our focus will be exclusively on the three suspensions of AuNSTs, AuNROs, and AuNFLs at 808 nm (see also ESI,† Fig. S7 and Table S1).

Table 2 gives the variation of the temperature, SAR values, the heating and cooling time coefficients, τ_h and τ_c, and the corresponding conversion efficiencies, η_h and η_c, for irradiation at 808 nm with different powers and gold concentrations. The temperature increments vary from about 9 °C for AuNROs at 0.05 Mm with the lower power to 45 °C for AuNSTs at 0.2 mM with the higher power. Within these limits there is no proportionality between the power, the concentration and the increment, though there is a tendency for the increment to increase with both of the former. The temperature increments and the SAR values increase in the order AuNRO < AuNFL ≈ AuNST (Fig. S8, ESI†). SAR tends to fall as the concentration increases at both wavelengths, with particularly high values at 0.05 mM, but is very irregular (Table 2). Values for the heating and cooling time coefficients vary very little with gold concentration and power, but the former are systematically lower than the latter. This can be explained by stronger heat dissipation because of plasmonic NP vibrations during laser irradiation. Consequently, those for the corresponding conversion efficiencies are also lower for cooling than for heating. Mean values of η for AuNROs and AuNSTs vary little with gold concentration, tending to decrease slightly as the gold concentration falls and, on average, depend little on the power, whereas for AuNFLs η increases as the concentration falls, leading to particular high values of about 80% for 0.05 mM suspensions at both powers. Although comparisons are difficult because of the different protocols, concentrations and sizes of nanoparticles, the values obtained for η are comparable with published results.[40–44] Overall, the ordering is slightly different from that of the SAR values: AuNRO < AuNST < AuNFL. A plausible explanation for the higher SAR and η for AuNFLs and AuNSTs lies in their larger specific surface areas. The porous structure of AuNFLs with multiple dendritic tips likely enhances light absorption and heat dissipation from the particles to the liquid phase. As the distances between particles decrease with increasing concentration, their interactions should be more pronounced, but it is not clear how this impacts the absorption efficiency and heat release of each particle. The contrasting results for AuNFLs and AuNROs/AuNSTs indicate that further research is needed to explore the interactions between nanoparticles and to gain a deeper understanding of the underlying physical mechanisms.

3.4 Antibacterial effect of AuNP suspensions on planktonic *Escherichia coli*

Escherichia coli (*E. coli*) is a common bacterium found in the intestines of humans and animals. However, certain strains can cause serious infections, leading to illnesses such as urinary tract infections, gastroenteritis, and even life-threatening conditions like sepsis.[45–47]

Bacterial growth occurs in two phases: the exponential phase, when bacteria are actively dividing, and the stationary phase, when the number of new cells produced balances the number of cells that die. Specifically, *E. coli* in the stationary phase is characterised by membrane rigidification and a slower metabolism, as a result of nutrient depletion. Thus, in this phase it is more tolerant to stresses by antibiotics, nanoparticles and heat.[30,48]

Stationary-phase planktonic *E. coli* were incubated with AuNPs of different morphologies for 1 hour at 37 °C, and photothermal treatment then performed by irradiating the *E. coli*/AuNP mixtures for 10 minutes at 808 nm (Fig. S8, ESI†). The temperature increments for the most effective AuNPs were very similar at around 27–30 °C while that for AuNSPs was only 10 °C (Table S2, ESI†). Corresponding survival rates, ($\log N$ (CFU mL^{-1})), $\Delta \log N$ (CFU mL^{-1}), and mortalities (Section 2.4.2.4) are displayed in Fig. 4a, b and Fig. S8 (ESI†). In the absence of irradiation, mortalities (Table S2, ESI†) increase in the order AuNSP (5%) < AuNRO (28%) < AuNFL (76%) < AuNST (98%), which highlights the importance of the intrinsic antibiotic capacity of the AuNPs, particularly those with the most complex structures. When samples were irradiated at 808 nm, mortalities for the most effective NPs rose to roughly 100%, with AuNSTs slightly more effective than AuNROs and AuNFLs, while that for AuNSPs rises to about 75%. This indicates even a low level of heating can increase the antibiotic efficacity.

Another way of looking at the data is to consider the reduction in $\log N$ (CFU mL^{-1}). Reductions by 1, 2, 3 and 4 log units correspond to mortalities of 90%, 99%, 99.9% and 99.99%, respectively. Any value over 3 is an indication of strong antibacterial activity. The $\log N$ (CFU mL^{-1}) of *E. coli* in the stationary phase, after contact with the AuNPs is represented in Fig. 3 and the values of the $\Delta \log N$ (CFU mL^{-1}) in Table S2 (ESI†). In the absence of photothermia, the bactericidal effect is low for any of the AuNPs, except AuNSTs, where $\Delta \log N$ (CFU mL^{-1}) is almost 2. AuNROs and AuNFLs show log reductions around 2 ($P < 0.01$). When photothermia is applied, AuNSTs show the best bactericidal effect, achieving a 3 to 4-log reduction ($P \leq 0.0001$). Clearly, this would be the best material for any

Fig. 4 (a) $\log N$ (CFU mL^{-1}) and (b) $\Delta \log N$ (CFU mL^{-1}) of *E. coli* in the stationary phase, after incubation with different AuNP suspensions (AuNSP–citrate, AuNRO–citrate, AuNFL–dopamine, and AuNST–PVP) followed or not by irradiation (808 nm, power: 0.5 W). All experiments were performed in triplicate; error bars indicate standard deviations. Significance: non-significant (ns) for $P > 0.05$, * for $P \leq 0.05$ (significant), ** for $P \leq 0.01$ (highly), *** for $P \leq 0.001$ (very highly), and **** for $P \leq 0.0001$ (extremely).

practical application of gold nanoparticles to the treatment of bacterial infections in the second biological window of the NIR.

4. Conclusion

The idea behind this work was to study the shape dependence of the photothermal and biocidal properties of AuNPs. To this end, four morphologies (spherical, rod-shaped, star-shaped, and flower-like, designated as AuNSP, AuNRO, AuNST, and AuNFL, respectively) were selected from the multitude of possibilities, and AuNPs capped in various ways and of different sizes were synthesised and characterised. The temperature increase upon irradiation at 808 nm was rather less for AuNSPs than for the other forms, while at 1064 nm the order was AuNSP $<$ AuNRO $\ll$ AuNFL $<$ AuNST. Photothermal conversion efficiencies are of the same order of magnitude as those reported for a wide variety of morphologies investigated with a view to application in inside-out tumor ablation, but strict comparisons are impossible because of differences in size, capping, concentration, experimental conditions and even

data-handling. Clearly, AuNPs have the ability to kill bacteria, and their efficacy is enhanced *via* PTT induced by NIR irradiation. However, due to the multiplicity of variables regarding the make-up of the different particles, it is not possible to attribute differences in efficacy to any one factor. The most one can say is that small spherical particles are very poor nano-heaters (at 808 nm and 1064 nm) and biocides, while larger rods, flowers and stars are very effective biocides under NIR-PTT conditions.

The present study demonstrates the differences in photo-thermal performance and *in vitro* biological efficacy of AuNPs with various morphologies. The experimental conditions make no attempt to simulate the complex biological *in vivo* environment. Many challenges remain. For instance, how can efficient targeting and photothermal conversion of nanoparticles in real biological environments be achieved? How can the antibacterial efficacy of nanoparticles be maximized without compromising biocompatibility? Addressing these questions will require collaboration across the fields of nanomaterials science, biomedical engineering, and biology. By conducting more rigorous experiments in 3D cell models for example, we can more accurately predict the clinical effectiveness of these nanoparticles.

Author contributions

M. H. conceived the entire project, supervised the experimental campaign, and handled project administration and funding acquisition. Z. P. performed all the experimental work (synthesis of AuNPs, assays, spectroscopy, photothermal and biological experiments, *etc.*). Y. L. and C. M. supervised the synthesis of AuNPs. M. B. and C. C.-G. participated to the interpretation of the results. P. D. performed the XPS analysis. S. G. D performed the SEM analysis. R. B. supervised the biological work. L. R. analysed the photothermal experiments. J. L. contributed to analysis and interpretation of results. M. H., J. L., Z. P. L. R., R. B., Y. L. and C. M. drafted, reviewed and edited the manuscript. All authors have read and agreed to the version of the manuscript submitted.

Data availability

The data supporting this article have been included as part of the ESI.†

Conflicts of interest

The authors declare that they have no known competing financial interests or personal relationships that could have appeared to influence the work reported in this paper.

Acknowledgements

References

1 M. Kus-Liśkiewicz, P. Fickers and I. Ben Tahar, *Int. J. Mol. Sci.*, 2021, **22**, 10952.

2 N. Singh, R. Sharma and R. Bharti, *Mater. Today Proc.*, 2023, **81**, 876–881.

3 P. Si, N. Razmi, O. Nur, S. Solanki, C. Mouli Pandey, R. K. Gupta, B. D. Malhotra, M. Willander and A. de la Zerda, *Nanoscale Adv.*, 2021, **3**, 2679–2698.

4 W. Wang, R. Dong, D. Gu, J. He, P. Yi, S.-K. Kong, H.-P. Ho, J. Loo, W. Wang and Q. Wang, *Adv. Med. Sci.*, 2020, **65**, 86–92.

5 C. J. L. Murray, K. S. Ikuta, F. Sharara, L. Swetschinski, G. R. Aguilar, N. Kissoon, E. Kobeissi, T. Kostyanev, F. Krapp, R. Krumkamp, C. Moore, C. Dolecek and M. Naghavi, *The Lancet*, 2022, **399**, 629–655.

6 M. M. Zafer, G. A. Mohamed, S. R. M. Ibrahim, S. Ghosh, C. Bornman and M. A. Elfaky, *Arch. Microbiol.*, 2024, **206**, 101.

7 J. Milan, K. Niemczyk and M. Kus-Liśkiewicz, *Materials*, 2022, **15**, 3355.

8 M. Lu, S. Li, Y. Liu, B. Xu, S. Liu, J. Zhang, D. Zhou and H. Liu, *Nano Today*, 2024, **57**, 102327.

9 C. Sahli, S. E. Moya, J. S. Lomas, C. Gravier-Pelletier, R. Briandet and M. Hémadi, *Theranostics*, 2022, **12**, 2383–2405.

10 C. Zhang, D.-T. Shi, K.-C. Yan, A. C. Sedgwick, G.-R. Chen, X.-P. He, T. D. James, B. Ye, X.-L. Hu and D. Chen, *Nanoscale*, 2020, **12**, 23234–23240.

11 P. P. Sarma, A. Rai and P. K. Baruah, *Antibiotics*, 2024, **13**, 124.

12 P. Manivasagan, F. Khan, D. Rajan Dhatchayeny, S. Park, A. Joe, H.-W. Han, S.-H. Seo, T. Thambi, V. H. Giang Phan, Y.-M. Kim, C.-S. Kim, J. Oh and E.-S. Jang, *J. Adv. Res.*, 2023, **48**, 87–104.

13 A. Hedaoo, P. Khairnar, G. Vambhurkar, D. A. Srinivasarao, M. Negi, A. Shinde and S. Srivastava, *Eur. Polym. J.*, 2024, **216**, 113282.

14 W. Bian, Y. Wang, Z. Pan, N. Chen, X. Li, W.-L. Wong, X. Liu, Y. He, K. Zhang and Y.-J. Lu, *ACS Appl. Nano Mater.*, 2021, **4**, 11353–11385.

15 G. Guan, K. Y. Win, X. Yao, W. Yang and M.-Y. Han, *Adv. Healthcare Mater.*, 2021, **10**, 2001158.

16 W. Yang, B. Xia, L. Wang, S. Ma, H. Liang, D. Wang and J. Huang, *Mater. Today Sustain.*, 2021, **13**, 100078.

17 Z.-R. Yang, H. Qin, J.-W. Fan, K. Du, L. Qi, D. Hou, H. Jiang and J. Zhu, *J. Colloid Interface Sci.*, 2024, **663**, 1074–1086.

18 R. Ranjana, N. Parushuram, K. S. Harisha, B. Narayana and Y. Sangappa, *Bionanoscience*, 2020, **10**, 864–875.

19 S. Anil Bansal, V. Kumar, J. Karimi, A. Pal Singh and S. Kumar, *Nanoscale Adv.*, 2020, **2**, 3764–3787.

20 M. L. Taylor, R. E. Wilson, K. D. Amrhein and X. Huang, *Bioengineering*, 2022, **9**, 200.

21 J. G. Mehtala, D. Y. Zemlyanov, J. P. Max, N. Kadasala, S. Zhao and A. Wei, *Langmuir*, 2014, **30**, 13727–13730.

22 J. Wan, J.-H. Wang, T. Liu, Z. Xie, X.-F. Yu and W. Li, *Sci. Rep.*, 2015, **5**, 11398.

23 Q. Zhong, J. Feng, B. Jiang, Y. Fan, Q. Zhang, J. Chen and Y. Yin, *J. Am. Chem. Soc.*, 2021, **143**, 20513–20523.

24 H. Chatterjee, D. S. Rahman, M. Sengupta and S. K. Ghosh, *J. Phys. Chem. C*, 2018, **122**, 13082–13094.

25 J. Hai, H. Piraux, E. Mazarío, J. Volatron, N. T. Ha-duong, P. Decorse, J. S. Lomas, P. Verbeke, S. Ammar, C. Wilhelm, J.-M. E. H. Chahine and M. Hémadi, *J. Mater. Chem. B*, 2017, **5**, 3154–3162.

26 Y. Luo, Y. Xiao, D. Onidas, L. Iannazzo, M. Ethève-quelquejeu, A. Lamouri, N. Félidj, S. Mahouche-chergui, T. Brulé, N. Gagey-eilstein, F. Gazeau and C. Mangeney, *Chem. Commun.*, 2020, **56**, 6822–6825.

27 K. Liu, Y. Zheng, X. Lu, T. Thai, N. A. Lee, U. Bach and J. J. Gooding, *Langmuir*, 2015, **31**, 4973–4980.

28 C. Sahli, J. Deschamps, L. Royon, J. S. Lomas, R. Briandet and M. Hémadi, *Mater. Today Chem.*, 2024, **35**, 101920.

29 H. Belkahla, R. Boudjemaa, V. Caorsi, D. Pineau, A. Curcio, J. S. Lomas, P. Decorse, A. Chevillot-biraud, T. Azaïs, C. Wilhelm, H. Randriamahazaka and M. Hémadi, *Nanoscale Adv.*, 2019, **1**, 2571–2579.

30 L. C. Gomes, J.-C. Piard, R. Briandet and F. J. Mergulhão, *LWT – Food Sci. Technol.*, 2017, **85**, 309–315.

31 R. Ahmad, L. Boubekeur-Lecaque, M. Nguyen, S. Lau-Truong, A. Lamouri, P. Decorse, A. Galtayries, J. Pinson, N. Felidj and C. Mangeney, *J. Phys. Chem. C*, 2014, **118**, 19098–19105.

32 R. del Caño, J. M. Gisbert-González, J. González-Rodríguez, G. Sánchez-Obrero, R. Madueño, M. Blázquez and T. Pineda, *Nanoscale*, 2020, **12**, 658–668.

33 J. Mosquera, D. Wang, S. Bals and L. M. Liz-Marzán, *Acc. Chem. Res.*, 2023, **56**, 1204–1212.

34 Á. I. López-Lorente and B. Mizaikoff, *TrAC, Trends Anal. Chem.*, 2016, **84**, 97–106.

35 X. Cui, Q. Ruan, X. Zhuo, X. Xia, J. Hu, R. Fu, Y. Li, J. Wang and H. Xu, *Chem. Rev.*, 2023, **123**, 6891–6952.

36 Z. Qiao, Y. Yao, S. Song, M. Yin, M. Yang, D. Yan, L. Yang and J. Luo, *J. Mater. Chem. B*, 2020, **8**, 3138–3149.

37 H. Belkahla, E. Mazarío, A. P. Sangnier, J. Lomas, T. Gharbi, S. Ammar, O. Micheau, C. Wilhelm and M. Hémadi, *Theranostics*, 2019, **9**, 5924–5936.

38 A. Paściak, R. Marin, L. Abiven, A. Pilch-Wróbel, M. Misiak, W. Xu, K. Prorok, O. Bezkrovnyi, Ł. Marciniak, C. Chanéac,

F. Gazeau, R. Bazzi, S. Roux, B. Viana, V.-P. Lehto, D. Jaque and A. Bednarkiewicz, *ACS Appl. Mater. Interfaces*, 2022, **14**, 33555–33566.

39 A. Paściak, A. Pilch-wróbel, Ł. Marciniak, P. J. Schuck and A. Bednarkiewicz, *ACS Appl. Mater. Interfaces*, 2021, **13**, 44556.

40 Y. Wang, Y. Yang, L. Yang, Y. Lin, Y. Tian, Q. Ni, S. Wang, H. Ju, J. Guo and G. Lu, *ACS Appl. Mater. Interfaces*, 2022, **14**, 28570–28580.

41 D. L. Amarasekara, C. S. Kariyawasam, M. A. Hejny, V. B. Torgall, T. A. Werfel and N. C. Fitzkee, *ACS Appl. Mater. Interfaces*, 2024, **16**, 4321–4332.

42 X. Wang, G. Li, Y. Ding and S. Sun, *RSC Adv.*, 2014, **4**, 30375–30383.

43 H. Chen, L. Shao, T. Ming, Z. Sun, C. Zhao, B. Yang and J. Wang, *Small*, 2010, **6**, 2272–2280.

44 H. S. Kim and D. Y. Lee, *Polymers*, 2018, **10**, 961.

45 J. R. Johnson and T. A. Russo, *J. Lab. Clin. Med.*, 2002, **139**, 155–162.

46 G. Shahbazi, M. A. Rezaee, F. Nikkhahi, S. Ebrahimzadeh, F. Hemmati, B. B. Namarvar and P. Gholizadeh, *Gene Rep.*, 2021, **25**, 101318.

47 Y. Zhou, Z. Zhou, L. Zheng, Z. Gong, Y. Li, Y. Jin, Y. Huang and M. Chi, *Int. J. Mol. Sci.*, 2023, **24**, 10537.

48 V. A. Veselovsky, M. S. Dyachkova, D. A. Bespiatykh, R. A. Yunes, E. A. Shitikov, P. S. Polyaeva, V. N. Danilenko, E. I. Olekhnovich and K. M. Klimina, *Microorganisms*, 2022, **10**, 1683.